

**1Effect of heat treatments on fabricated Wire and arc
2additive manufacturing parts of Stainless steel 316:
3Microstructure and synchrotron X-ray Diffraction
4analysis**

**5Authors: Tiago A.Rodrigues ^{a*} , J. D. Escobar ^d, Jiajia
6Shen ^a, Valdemar R. Duarte ^a, G. G. Ribamar ^b, Julian
7A. Avila ^b, Emad Maawad ^c, Norbert Schell ^c, , Telmo G.
8Santos ^a, J. P. Oliveira^{a ,1, #}**

^{9a} UNIDEMI, Department of Mechanical and Industrial Engineering, NOVA School of Science and Technology,
¹⁰Universidade NOVA de Lisboa, 2829-516 Caparica, Portugal

^{11b} São Paulo State University (UNESP), Campus of São João da Boa Vista, Av. Profª Isette Corrêa Fontão, 505, Jardim das
¹²Flores, 13876-750, São João da Boa Vista, SP, Brazil

^{13c} Helmholtz-Zentrum Geesthacht, Institute of Materials Research, Max-Planck-Str. 1, Geesthacht, 21502, Germany

^{14d} Metallurgical and Materials Engineering Department, University of São Paulo, Av.Prof. Mello Moraes 2463, 05508-030,
¹⁵São Paulo, SP, Brazil

^{16*}Corresponding author at tma.rodriques@campus.fct.unl.pt

^{17#} Corresponding author at jp.oliveira@fct.unl.pt

18Abstract

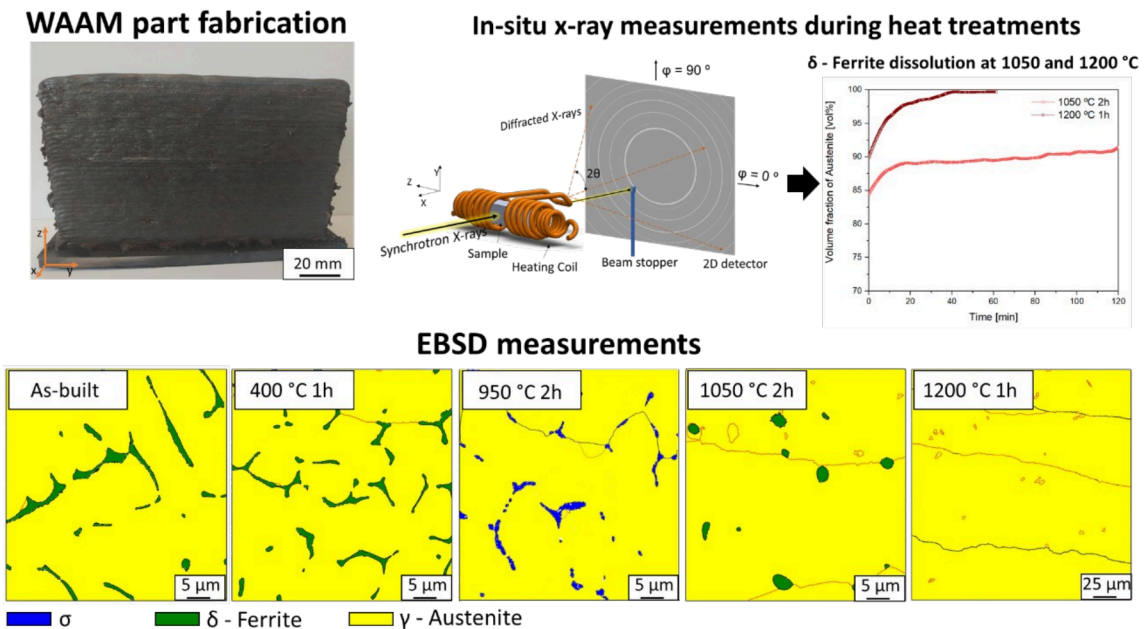
¹⁹Different geometrical features and intricate parts can now be fabricated by wire and arc
²⁰additive manufacturing (WAAM). Even though a broad range of applications rises with this
²¹technology, the processed metallic materials still follow metallurgy rules. Therefore, undesired
²²phases may appear during the multiple thermal cycles affecting the fabricated part. One of the
²³most used stainless steel in the industry is the 316L, which provides a combination of high
²⁴corrosion resistance and mechanical properties. In this study, 316L stainless steel walls were
²⁵fabricated by WAAM and submitted to several heat treatments to understand the precipitation
²⁶kinetics of secondary phases and observe the δ -ferrite dissolution with synchrotron X-ray
²⁷diffraction measurements. The as-built samples presented δ -ferrite dendrites in an austenite

¹¹ **Statement on Conflicts of Interest:** One of the authors of this article is part of the Editorial Board of
²the journal. To avoid potential conflicts of interest, the responsibility for the editorial and peer-review
³process of this article lies with the journal's other editors. Furthermore, the authors of this article were
⁴removed from the peer review process and had no, and will not have any access to confidential
⁵information related to the editorial process of this article.

28(γ) matrix. In-situ observations showed σ precipitation during the first minutes of isothermal
 29holding at 950 °C, from direct precipitation on the δ -ferrite islands. Solubilization heat
 30treatments at 1050 and 1200 °C resulted in an undissolved amount of ferrite of approximately
 316.5 % and 0.4 %, respectively. The amount of δ -ferrite showed a direct relationship with the
 32hardness values. This work combined advanced materials characterization and thermodynamic
 33calculations to rationalize the microstructure evolution upon the use of heat treatments in
 34WAAM-fabricated 316L stainless steel parts.

35**Keywords:** wire and arc additive manufacturing; stainless steel; sigma phase; in-situ phase
 36transformation, high energy synchrotron x-ray diffraction

37 Graphical Abstract



38

39 Highlights

- 40 • Different heat treatments were performed on stainless steel 316L WAAMed parts
- 41 • σ precipitation is observed in-situ via high energy synchrotron X-ray diffraction
- 42 • σ starts to precipitate during the first minutes of isothermal holding at 950 °C in the δ -
 43 ferrite grains
- 44 • The amount of δ -ferrite decreased with an increase in the solubilization temperature.
- 45 • Eddy current testing is capable to differentiate δ -ferrite and σ .

46

47 **1. Introduction**

48 Austenitic stainless steels are widely used in several industrial applications where exceptional
49 corrosion resistance and excellent mechanical properties at elevated temperatures is a
50 requirement, including nuclear energy [1,2] petrochemical, and chemical industries [3]. For
51 example, parts from a reactor core in nuclear applications are exposed to high strength and
52 corrosion environments at operating temperatures between 280-550°C [4,5]. The mechanical
53 strength of austenitic stainless steels is reduced considerably above 500°C [6], and the fatigue
54 crack propagation accelerates under operational temperatures above 150°C [7]. Austenitic
55 stainless steels are also an economical structural material used for marine and biomedical
56 applications [8,9].

57 Stainless steels are relatively expensive to machine from a billet, therefore complex parts are
58 more feasible and cheaper to fabricated with additive manufacturing technologies. Regarding
59 additively manufactured samples of austenitic stainless steels, Lou et al. [10] highlight the
60 necessity of producing an equiaxed microstructure through high-temperature recrystallization
61 annealing, which increases the corrosion fatigue resistance.

62 Wire and arc additive manufacturing (WAAM) is a variant within the metal additive
63 manufacturing group, based on the fundamentals of arc welding [11], where a wire feedstock
64 material is melted by an electric arc and deposited in a layer-by-layer fashion. WAAM features
65 high deposition rates and high material efficiency (less material waste), which is interesting for
66 building large components for industrial applications, such as for the oil and gas, and nuclear
67 sectors.

68 Austenitic stainless steels manufactured by WAAM typically exhibit δ -ferrite dendrites within
69 an austenitic (γ) matrix [12]. Some authors found that δ -ferrite can prevent hot cracking by
70 accommodating large amounts of pure S and P in the interdendritic areas [13–16] while also
71 acting as a strengthener. The multiple heating/cooling cycles experienced during WAAM of
72 austenitic stainless steel, combined with the long soaking times at high temperatures, affect
73 the microstructure evolution in WAAM fabricated parts, and can result in the formation of
74 undesired secondary phases [17]. When austenitic stainless steels experiences low cooling
75 rates and long times between 550-900 °C, Cr-rich carbides ($M_{23}C_6$ and M_7C_3) [18] will form, as
76 well as the potential for precipitating intermetallic deleterious phases increases, such as sigma
77 (σ) [19], chi (χ) [20–22], and Laves [18]. Especially regarding WAAM, it has been largely
78 reported that the as-fabricated microstructures in austenitic stainless steels, as a result of

79microsegregation of Cr during solidification can contain σ [23,24]. depending on the process
80parameters and location within the sample. The σ phase leads to hardening and embrittlement
81in stainless steel and therefore has received particular attention [25,26]. In addition, σ
82consumes chromium and molybdenum from the austenite matrix, deteriorating its corrosion
83resistance [27].

84The solidification conditions and multiple heating/cooling cycles during fusion based additive
85manufacturing can render different microstructure features when compared to conventionally
86used processes such as casting. The commonly used heat-treatments for welding and wrought
87material may also need to be adapted when producing WAAM parts. Some authors [28] have
88suggested that at 950 °C δ -ferrite could dissolve without the precipitation of secondary phases
89after post-weld heat treatment. As it will be shown in this work, the same heat treatment
90condition when applied to the WAAM 316L stainless steel parts will render different
91microstructure features.

92It has been also discussed that δ -ferrite can serve as nucleation sites for the precipitation of
93 $M_{23}C_6$ and σ upon annealing cycles around 720 °C. However, proper annealing cycles around
941050 °C can provide complete dissolution of δ -ferrite, avoiding the formation of secondary
95precipitates [29]. The presence of compositional segregations and δ -ferrite are mostly
96unavoidable and therefore understanding the microstructural evolution of as-built austenitic
97stainless steels after WAAM heat treatment is currently a topic of great interest for the additive
98manufacturing community. In-situ synchrotron X-ray diffraction measurements are especially
99useful in this case to understand the kinetics of phase transformations during heat treatments.

100This study investigates the phase transformations in a 316L austenitic stainless steel after
101WAAM using synchrotron X-ray diffraction. The kinetics of δ -ferrite dissolution was studied
102during post-WAAM heat treatment at 400, 950, 1050, and 1200 °C. The selection of these heat
103treatments was made base on the literature [23,30–32]. Complementary EBSD analysis was
104performed to confirm the morphology, size, and distribution of δ -ferrite and σ before and after
105heat treatment. Eddy's current testing was used to highlight that δ -ferrite can be distinguished
106from σ with this technique. While hardness and electrical conductivity measurements were
107used to demonstrate the differences that each phase can have on the final properties of the
108processed materials. Our observations provide a new understanding of the effects of time and
109temperature on the microstructural evolution of as-built austenitic stainless steels after WAAM

110and provide a useful guide to design or optimize heat treatment routes relevant to additively
111manufactured parts.

112**2. Materials and methods**

113**2.1 Experimental setup**

114In this study, WAAM single-walls were fabricated using an in-house custom-made WAAM
115apparatus, which included a customized gas metal arc welding (GMAW) torch. The wire
116feedstock used in this work was a commercial 316L stainless steel wire (ER 316LSi) with a
117diameter of 1 mm. The chemical composition of the feedstock wire is detailed in Table 1. A
118WAAM wall with 180 x 110 x 8 mm was built with a wire feed speed of 4 m/min and a travel
119speed of 300 mm/min. A voltage of 19.5 V was used, and the molten pool was protected with
12099.99 % Argon. A zig-zag deposition strategy with 90 seconds of idle time between each torch
121stop/start was selected to build the 75-layer WAAM part.

122 *Table 1 - Chemical composition of the ER 316LSi wire electrode (wt.%).*

C	Mn	Si	Ni	Cr	Mo	Cu	Fe
0.03	1.60	0.65	11	18.5	2.50	0.75	Bal.

123

124**2.2 In-situ synchrotron x-ray diffraction during heat 125treatments**

126Four post-WAAM heat treatments (PWHT) were performed in-situ at the High Energy Materials
127Science beamline at PETRA III, DESY (Hamburg, Germany) with a beam energy of 100 keV
128(0.1234 Å). Material expansion/shrinkage during heating and cooling was measured using a
129modified Bähr DIL-805 dilatometer filled with Argon to avoid oxidation during the heat
130treatments.

131The four different heat treatments were performed as follows: HTT#1 consisted of a stress
132relief heat treatment at 400 °C for 1 hour, followed by air cooling; HTT#2 aimed at promoting σ
133precipitation and was performed at 950 °C for 2 hours, followed by forced gas (Ar) cooling;
134HTT#3 was performed at 1050 °C for 2 hours, followed by forced gas (Ar) cooling; while HTT#4
135was performed at 1200 °C for 1 hour, also followed by forced gas (Ar) cooling. It should be
136noticed that the selection of imposing forced gas cooling aimed at avoiding the precipitation of

137intermetallics after the termination of the high-temperature plateau. All conditions were
138heated up to the target treatment temperature at a rate of 20 °C/s. As for the cooling
139conditions, HTT#1 had a cooling rate of 5 °C/s, while for the remaining heat treatments, a
140cooling rate of 20 °C/s was imposed.

141A schematic representation of the heat treatments performed and the in-situ setup used are
142depicted in Figure 1 and Figure 2. The primary purpose of the synchrotron experiments was to
143determine the δ -ferrite dissolution and the kinetics of secondary phase formation/dissolution
144during the selected heat treatments.

145A 2D Perkin Elmer detector with a pixel size of 200 μm was used to capture the Debye-Scherrer
146diffraction rings. These were then integrated along the full azimuthal angle (ϕ) using freely
147available Fit2D software [33] to obtain conventional (Intensity vs. d-spacing) diffraction
148patterns. The beam size was 1 x 1 mm, and the sample-to-detector distance was set to 1517
149mm. LaB₆ calibrant powder was used to estimate the instrumental peak broadening associated
150with the beamline, and the exposure time was set to 5 seconds. During the in-situ
151measurements, dark images were also acquired and subtracted to reduce the noise of the
152detector images.

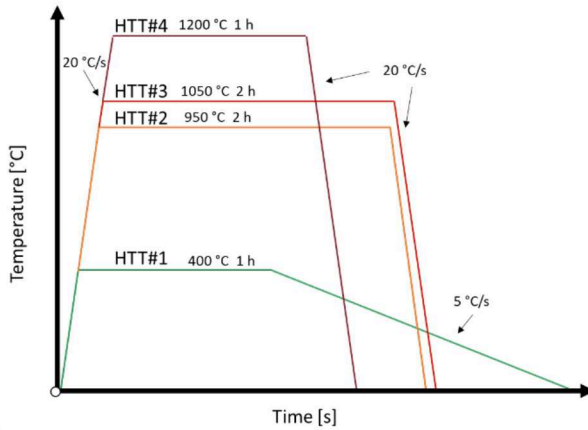
153An in-house python-based routine was used to fit the diffraction peaks. The python routine
154used a Python package named *xrdfit* [34], which implemented a *Pseudo-Voigt* profile function
155to fit peaks and extract the analyzed data in this study, i.e., the peak position, full width half
156maximum, and area under the fitted peaks. This information was then used to quantify the
157current phases at any given point during the heat treatments, following Escobar et al.[35]
158methodology. The austenite and ferrite volume fractions were measured using equations (1)
159and (2). F_p is the fraction of austenite/ferrite, n_p is the number of peaks of austenite/ferrite
160considered, k represents each {hkl} family/peak, I_{pk} the intensity of each peak, and R_{pk} is a
161scalar containing the effect of the remaining parameters: theoretical cell volume (V_p), the
162multiplicity of the peak (M), and the structure factor (F_k) of the {hkl} plane family. The R_{pk} was
163calculated for all presented phases of austenite and ferrite. The peaks tracked were: δ {220}, γ
164{222}, γ {311}, δ {211}, γ {220}, δ {200}, γ {200}, δ {110}, γ {111}. The final volume fraction of
165austenite was calculated following equation (3). This method to quantify the volume fraction of
166each phase was compared with actual Rietveld refinements measurements, using MAUD
167software [36]. The lattice strain for certain (h k l) peaks was calculated accordingly equation (4).
168The d-spacing of the as-built sample was considered as d_0 .

$$F_p = \frac{\frac{1}{n_p} \sum_K \frac{I_{pk}}{R_{pk}}}{\sum_p \frac{1}{n_p} \sum_K \frac{I_{pk}}{R_{pk}}} \quad (1)$$

$$R_{pK} = \frac{F_k^2 \times M}{V_p^2} \quad (2)$$

$$F_{p_{austenite}} = \frac{F_{p_{austenite}}}{F_{p_{austenite}} + F_{p_{ferrite}}} \quad (3)$$

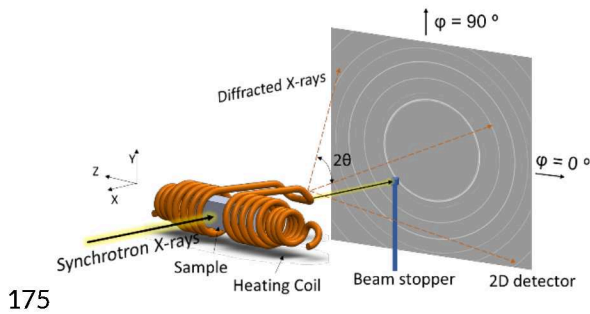
$$\text{Lattice strain}_{hkl} = \left(\frac{d - d_0}{d_0} \times 10^6 \right)_{hkl} \quad (4)$$



170

171 Figure 1 - Schematic representation of the heat treatments applied during In-situ Synchrotron
 172 X-ray diffraction measurements. The time-temperature plot also resumes the heating and
 173 cooling ramps used.

174



176 Figure 2 - Schematic representation of the experimental setup applied to perform the in-situ
177 heat treatments.

178

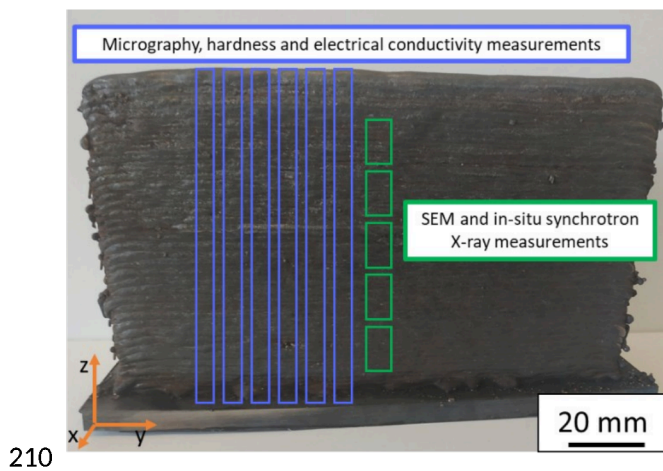
179 2.3 Microstructural characterization

180 All conditions, including the as-built WAAM walls, were analyzed via optical and scanning
181 electron microscopy, hardness testing, and electrical conductivity measurements. For the
182 microscopy observations, samples were polished using abrasive papers with grit from 80 to
183 2000 and polished using a 3 μm diamond suspension. Vilella's reagent was used to reveal the
184 microstructure. A Leica DMI 5000 M optical microscope and an FEI Quanta FEG - Inspect-F50
185 scanning electron microscope equipped with an electron backscatter diffraction (EBSD) camera
186 were used in this investigation. A python-based routine was used to calculate the percentage of
187 each phase based on at least three optical microscopy images on the microstructure images.
188 From this routine, the average and associated standard deviations were determined. EBSD
189 measurements were carried out using an acceleration voltage of 20 kV and a step size of 150
190 nm.

191 Hardness measurements were performed using a Mitutoyo HM-112 Hardness Testing Machine,
192 under a load of 0.5 N for 10 s across the sample's total height, with a distance between
193 indentations of 500 μm. Magnetic permeability measurements were performed using an
194 absolute helically shielded eddy current (EC) probe with a 3 mm diameter, operating in
195 bridge mode [37]. The electrical impedance was calibrated with different magnetic
196 permeability standards (ferrite samples), to distinguish between different materials with
197 unknown magnetic permeabilities. The calibration was performed so that only the imaginary
198 part of the electrical impedance of the probe conferred changes in the magnetic permeability
199 of each sample. To measure the changes in electrical conductivity between samples, a four-
200 point potential drop technique previously described in Sorger et al. [38] was used.
201 Measurements were made across the full height, starting in the substrate. Because the

202selected heat treatments are expected to promote microstructure changes it is important to
203evaluate how other properties of interest evolve upon those heat treatment schedules. Both
204hardness and electrical conductivity measurements can provide an indirect sense of the
205microstructural changes across the height of the samples as a function of the selected heat
206treatment [17]. The probe has a needle spacing of 635 μm , and a current of 80 mA was
207imposed between the external needles.

208Figure 3 details the position within a given WAAM wall where specimens were taken for
209microstructure and mechanical characterization.



211Figure 3 - Localization of the specimens taken from the Stainless steel 316 part, for
212microstructure and mechanical characterization.

213

214**3. Results and discussion**

215**3.1 Macroscopic characterization**

216Figure 4 a) shows a micrograph of the as-built sample with primary dendrites composed of δ -
217ferrite aligned with the solidification direction (z-axis). Micrographs of the produced samples
218are depicted in Figure 4 b) to f). The as-built condition (Figure 4 b) is characterized by δ -ferrite
219dendrites oriented perpendicular to the deposition direction in an austenitic (γ) matrix. After
220the stress relief heat treatment, the microstructure maintained similar characteristics to that of
221the as-built condition (Figure 4 c). With the increase in the heat treatment temperature to
2221050 $^{\circ}\text{C}$, the columnar features became more unnoticeable, with the dissolution of dendrites
223arms (Figure 4 e). Finally, when the heat treatment was set to 1200 $^{\circ}\text{C}$, almost no evidence of

224the original solidification microstructure of the as-built material exists. Only some tiny islands
225of residual ferrite dispersed in the matrix are depicted (refer to Figure 4 f).

226Figure 4 a) depicts a variation in the morphology of ferrite as the number of layers increases.
227Typically, layers comprise skeletal-type ferrite in the non-remelted area and lathy-ferrite in the
228remelted area between layers [23,39], which is explained by the higher cooling rates in the
229remelted zone, since it is the first portion of volume to solidify [40].

230Stainless steels solidify in one of four possible ways: mode A - single-phase austenite (Liquid \rightarrow
231Liquid + $\gamma \rightarrow \gamma$); mode AF - austenite with secondary ferrite (Liquid \rightarrow Liquid + $\gamma \rightarrow$ Liquid + γ + δ
232 $\rightarrow \gamma$ + δ); mode FA - primary ferrite with secondary austenite (Liquid \rightarrow Liquid + $\delta \rightarrow$ Liquid + δ
233+ $\gamma \rightarrow \delta$ + γ); and mode F - single-phase Ferrite (Liquid \rightarrow Liquid + $\delta \rightarrow \delta$) [40]. The
234determination of the solidification mode can be based on the chromium to equivalent nickel
235ratio Cr_{eq}/Ni_{eq} . For the material used in this work, the Cr_{eq}/Ni_{eq} ratio is 1.69 and, considering
236Schaeffler's diagram, a ferritic-austenitic (FA) solidification mode is present. The solidification
237microstructure should be composed of austenite with a ferrite content ranging from 5 to 10 %.
238Under equilibrium solidification conditions, the austenitic stainless steel should present a
239ferritic-austenitic (FA) solidification mode, in which δ -ferrite is the leading phase, and austenite
240(γ) is the second phase that begins to form between the liquid and δ -ferrite dendrites in a
241peritectic reaction [41]. Austenite will continue to solidify from the rest of the melt afterward.
242The diffusion-controlled δ -ferrite to austenite transformation will continue during cooling and
243stop when the diffusion is no longer possible, resulting in a skeletal and lathy ferrite type [42].

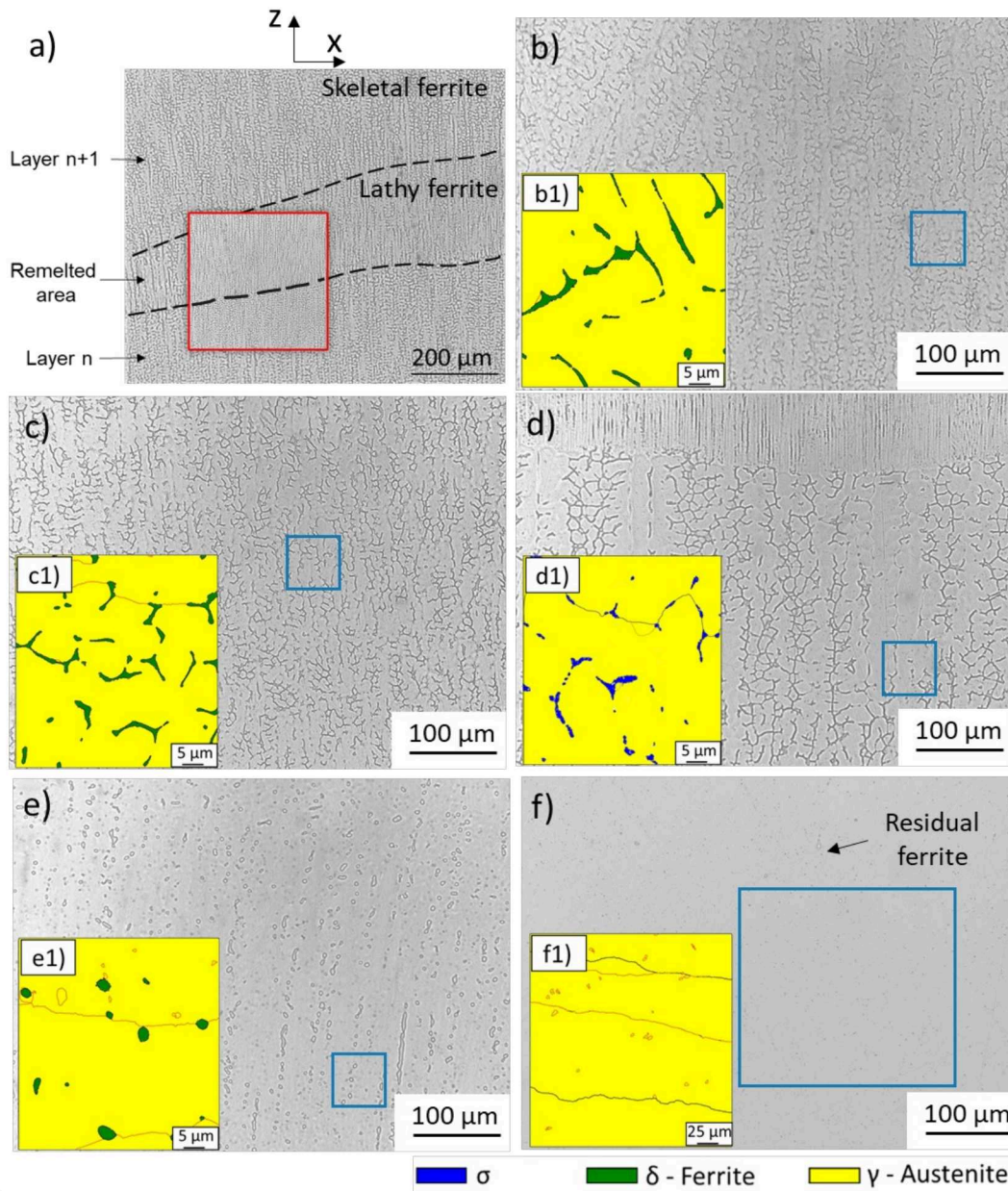


Figure 4 – a) and b) As-built, c) 400 °C 1h, d) 950 °C 2h, e) 1050 °C 2h f) 1200 °C 1h. Inserts b1, c1, d1, e1 and f1 correspond to the high magnification EBSD analysis.

3.2 Electron backscatter diffraction analysis

Figure 4 inserts depict the electron backscatter diffraction (EBSD) phase maps for each condition. As-built and stress relieved (400 °C / 1h) samples contain vermicular-type ferrite dispersed in the austenite matrix. The sample heat-treated at 950°C exhibits σ both in a vermicular-type structure and along the grain boundaries. The increase in the temperature to

2531050 °C revealed a lower fraction and size of δ -ferrite, as only small islands are present. In the
2541200 °C condition, δ completely disappeared from the WAAMed stainless steel part.

255Sigma (σ) can take up to thousands of hours to precipitate directly from austenite [24]. Padilha
256et al. [44] found in a creep test performed at 600 °C, that σ precipitation in austenite only
257occurred after 5481 h. The following reasons explain the low kinetics of σ precipitation from
258austenite: i) low solubility of C and N within the σ , which causes carbides and nitrides to form
259instead of promoting the σ transformation; ii) very slow diffusion of substitutional elements in
260austenite; and iii) different crystal structures between σ and austenite, which hinders
261nucleation of the former. This lack of lattice coherence, as well as the high interfacial energy
262between both phases, is the reason that leads to increased interface cracking when σ is
263present in these materials [26]. Contrarily, the σ was found to precipitate very quickly from
264residual δ -ferrite [13]. It prefers high Cr-concentrated regions, present in higher quantities in
265 δ -ferrite can diffuse easily in its BCC structure [45].

266Perron et al. [19] proposed three mechanisms for the precipitation of σ : i) it involves nucleation
267at the γ/δ interface, which is a high interface energy site place beneficial for heterogeneous
268nucleation, and also a high Cr-region; ii) direct precipitation in the corners or triple points in the
269 δ - ferrite, resulting from the Cr, Mo, and Ni concentration profiles; iii) eutectoid
270decomposition of δ -ferrite onto the σ and austenite ($\delta \rightarrow \sigma + \gamma$). Other nomenclatures exist;
271however, this partitioning is very similar to the one already described in the literature [26,46].

272Due to the preservation of the ferrite vermicular-type showed in the micrographs and the EBSD
273maps (refer to Figure 4 d) it can be perceived that the appearance of σ results from direct
274precipitation on the δ -ferrite islands. By precipitating within the δ -ferrite, the σ consumes the
275Cr content and ultimately occupies the entire δ -ferrite islands.

276The percentage of δ -ferrite and σ content was calculated from the optical microscope images
277previously depicted in Figure 4 with a Python routine, and the results are presented in Table 2.
278The percentage of δ -ferrite in the as-built sample, heat-treated at 400 °C, and heat-treated at
2791050 °C sample, is respectively 16.9, 17, and 2.8 %. The percentage of σ in the sample heat-
280treated at 950 °C is around 16.8 %. Regarding the undissolved δ -ferrite in the sample heat-
281treated at 1200 °C, the δ -ferrite is below 0.5 %.

282 Table 2 – Phase percentage measurements made with a Python routine of each phase based
 283 on three different micrographs of each condition.

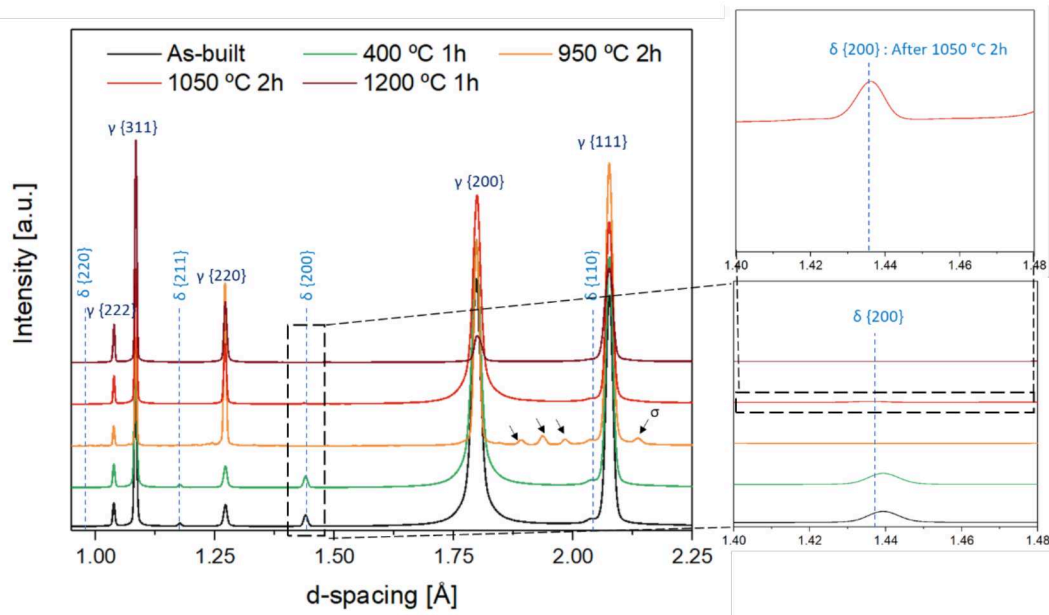
Condition	Austenite (γ)	δ -Ferrite	σ
As-built	83.1	16.9	-
400 °C 1h	83	17	-
950 °C 2h	83.2	-	16.8
1050 °C 2h	97.2	2.8	-
1200 °C 1h	99.5	0.5	-

284 3.3 Synchrotron X-ray diffraction analysis

285 3.3.1 Ex-situ microstructural characterization

286 Figure 5 depicts the diffraction patterns of the as-built sample and those after completion of
 287 the selected heat treatments. In the as-built sample, diffraction peaks corresponding to the
 288 austenite and ferrite phases are identified. Even though WAAM parts are kept at high
 289 temperatures for long periods during fabrication, no carbides or other undesirable phases than
 290 δ -ferrite were detected in the as-built sample.

291 Precipitation of σ was confirmed after two hours at 950 °C. Multiple diffraction peaks
 292 corresponding to σ are evidenced in the orange spectra of Figure 5. An apparent reduction in
 293 the intensity of the δ -ferrite peaks is observed after heat treatment at 1050 and 1200 °C. The
 294 insert in Figure 5 illustrates that δ -ferrite is still present after being heat-treated at 1050 °C.



295

296 Figure 5 - Overview of the diffraction patterns of the as-built and heat-treated samples. Inserts
 297 illustrate the existence of δ -ferrite after being heat-treated for two hours at 1050 °C.

298 Table 3 shows the evolution of the d-spacing for several diffraction peaks of both austenite and
 299 ferrite phases after the stress-relief heat treatment. It is interesting to note the shift of both
 300 ferrite and austenite peaks to higher d-spacing values (or correspondingly to lower scattering
 301 angles), indicating a change in the microstrain state, as typically for post-processing heat
 302 treatments [47].

303 **Table 3 - d-spacing values and lattice strain of the main austenite and δ -ferrite peaks before**
 304 **and after stress-relief heat treatment (400 °C for 1 h).**

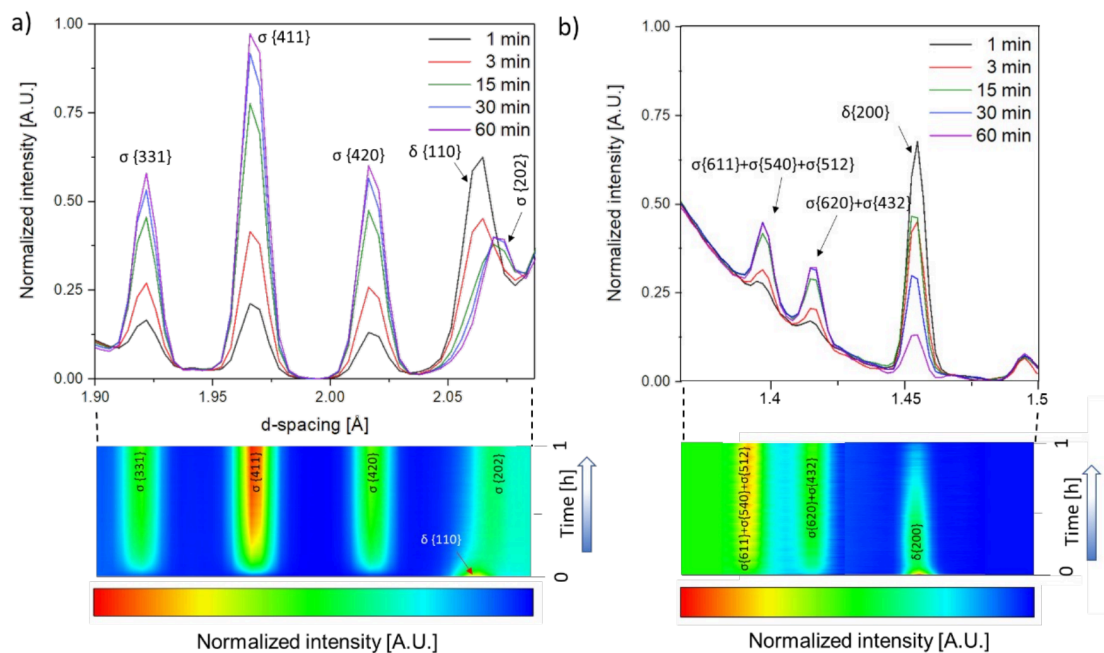
Peak	d-spacing [Å]	d-spacing [Å]	Lattice strain
	As-built	Stress-re- lief	
γ {311}	1.0835	1.0845	922
δ {211}	1.1742	1.1758	1362
γ {220}	1.2709	1.2714	393
δ {200}	1.4362	1.4397	2437
γ {200}	1.7967	1.7983	891
δ {110}	2.0413	2.0435	1078
γ {111}	2.0742	2.0810	3278

305 3.3.2 In-situ phase transformations

- 306 • Precipitation of σ from δ -ferrite at 950 °C

307 Figure 6 a) details the evolution of several diffracted σ planes ($\{202\}_\sigma$, $\{420\}_\sigma$, $\{411\}_\sigma$, and $\{311\}$
 308 σ) during the first hour of isothermal holding at 950 °C. These results were retrieved after
 309 isolating portions of the spectra containing a large density of σ peaks. To obtain a kinetic
 310 observation of σ precipitation, intensity was normalized based on the last observed $\sigma\{411\}$
 311 peak intensity at the end of the isothermal stage. Notice that the intensity of σ peaks is too
 312 small to obtain reliable sequential fitting. Therefore, a semiquantitative approach to σ
 313 precipitation kinetics and dissolution of δ can be obtained by this method. In this experiment,
 314 it was observed that the σ started to precipitate during the first minute at isothermal holding.
 315 Qualitatively it was observed in Figure 6 a) that after 15 minutes of heat treatment at 950 °C,
 316 the $\{110\}_\delta$ peak disappeared and the $\{202\}_\sigma$ overlapped. However, due to the peak broadening
 317 of the σ reflection, which decreases over time, and due to the existence of $\{200\}_\delta$ peak after 60
 318 minutes (refer to Figure 6 b), it is evidenced that the partial transformation of ferrite to σ was
 319 unfinished after 15 minutes.

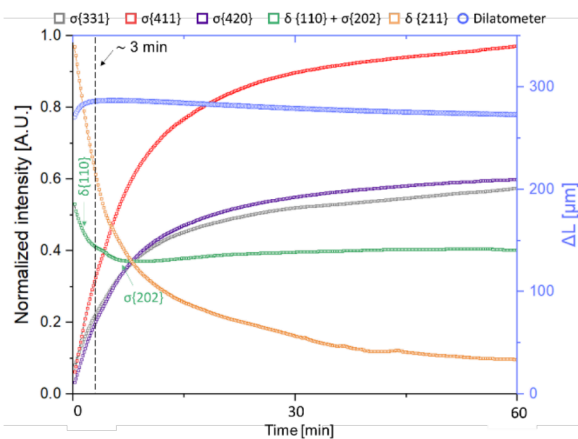
320 The final amount of σ is highly dependent on the starting amount of δ -ferrite since σ
 321 preferentially forms in the δ -ferrite regions (Figure 4). These results highlight the importance of
 322 controlling the processing temperatures during WAAM to minimize the permanence times at
 323 high temperatures, hence preventing δ -ferrite amount and the precipitation of undesirable
 324 phases, such as σ , during subsequent heat treatments.



325

326 Figure 6 - a) and b) - Sigma (σ) growth and δ -ferrite dissolution in the isothermal stage at 950 °C
 327 after 1 min, 3 min, 15 min, 30 min, and 60 min. Peak intensity normalization of these two
 328 regions of the spectra (where a high density of σ peaks are observed) is conducted based on
 329 the maximum intensity of the $\{411\}_\sigma$ peak. Therefore, green-to-red colors represent the relative
 330 kinetics of precipitation of σ , while blue denotes the constant normalized background counts.

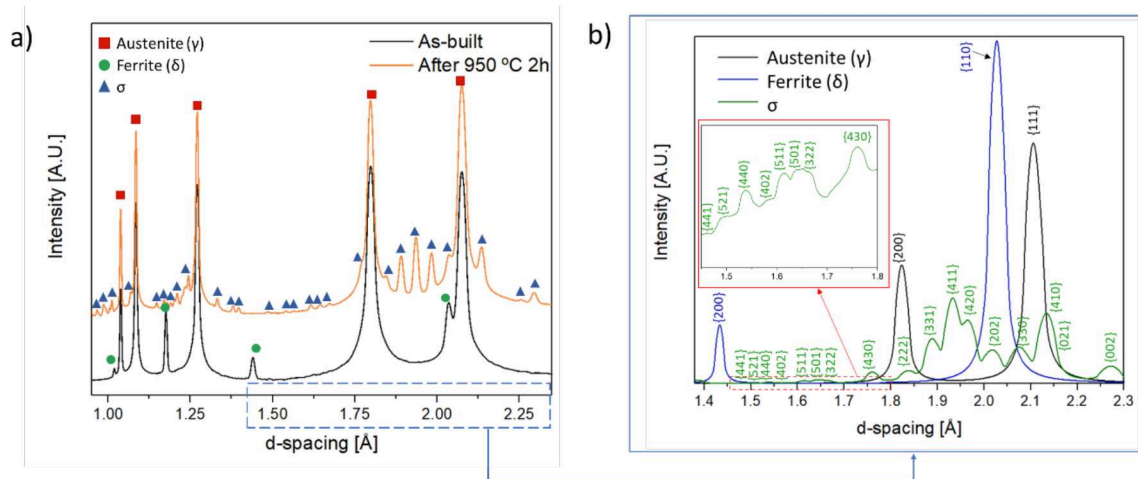
331 The dilatometry results of the first hour of the heat treatment performed at 950 °C are de-
 332 picted in Figure 7. The peak intensity evolution is based on the normalized intensity plot shown
 333 in Figure 6 a). The observed behavior illustrates a slight contraction in the sample during the
 334 first hour of isothermal holding. Rivolta et al. [48] showed that σ precipitation from δ -ferrite
 335 leads to a slight contraction in the dilatometric curve. The increase in σ peak intensity and the
 336 continuous dissolution of δ ferrite indicate a constant transformation of δ to σ during the
 337 isothermal stage of the heat treatment at 950 °C. The fast kinetics of δ to σ transformation indi-
 338 cates that σ -growth is likely to be controlled by a small-scale atomic rearrangement of BCC into
 339 the tetragonal crystal structure, instead of long-range diffusion of substitutional alloying ele-
 340 ments [49].



341

342 Figure 7 - Intensity evolution of the peaks $\{110\}_\delta$, $\{211\}_\delta$, $\{331\}_\sigma$, $\{411\}_\sigma$, $\{420\}_\sigma$ and $\{202\}_\sigma$
 343 during the first hour of the isothermal holding at 950 °C. The apparent stabilization of the
 344 $\{110\}_\delta$ peak after 3 minutes of isothermal dissolution is explained by the simultaneous
 345 precipitation of $\{202\}_\sigma$. This does not occur for $\{110\}_\delta$. The initial volumetric expansion is then
 346 associated with the dissolution of δ -ferrite. Precipitation of σ results in a modest volumetric
 347 contraction.

348 After the two hours of heat treatment, no δ -ferrite peaks were found, as detailed in Figure 8
 349 a). The large density of σ -phase precipitate peaks and the convolution of $\{110\}_\delta$ and $\{202\}_\sigma$
 350 peaks are shown in a simulated XRD spectrum in Figure 8 b).

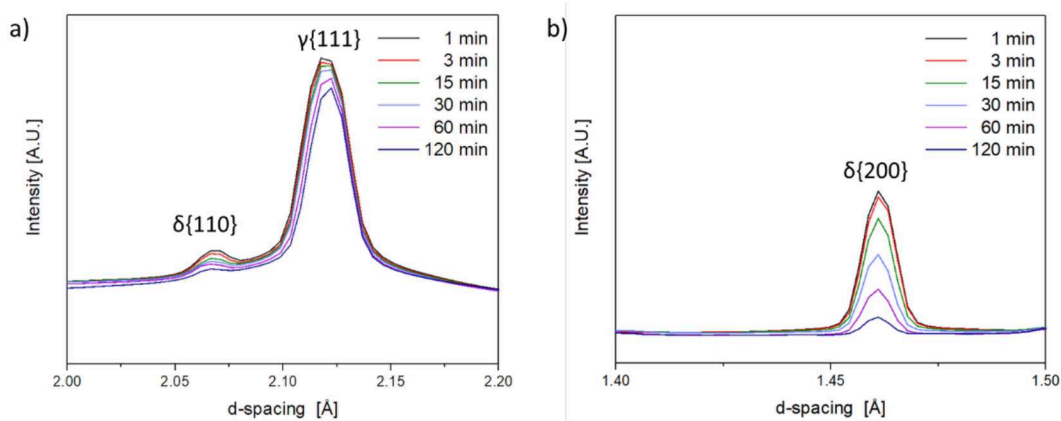


351

352 **Figure 8 - a) Overall overview of the powder pattern before and after heat treatment for 2**
 353 **hours at 950 °C.; b) Powder diffraction pattern of austenite, δ-ferrite, and σ.**

- 354 • Dissolution of δ-ferrite at 1050 and 1200 °C

355 Figure 9 depicts the evolution of $\{111\}_\gamma$, $\{110\}_\delta$ and $\{200\}_\delta$ peaks during isothermal holding at
 356 1050 °C for 120 minutes. The reduction in the scattered intensity of ferrite is accompanied by a
 357 decrease in the austenite reflection intensity. A texture change can explain this since no other
 358 compounds were formed during this heat treatment. Both solubilization heat treatments did
 359 not reveal any σ precipitation.



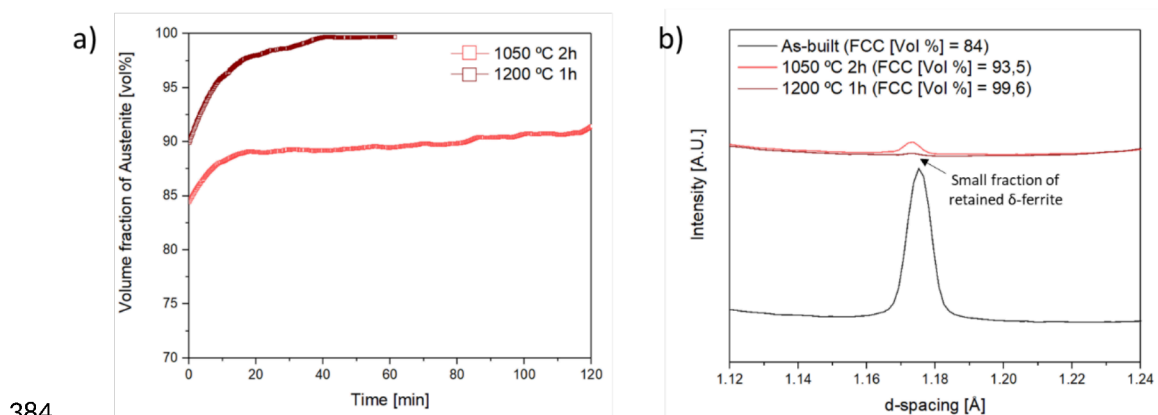
360

361 **Figure 9 - δ-Ferrite dissolution after isothermal holding at 1050 °C for 1 min, 3 min, 15 min, 30**
 362 **min, 60 min, and 120 min.**

363 To monitor the dissolution of the ferrite during the post-WAAM heat treatments, the scattered
 364 intensity, full width at half maximum (FWHM), and area of the fitted peaks of the FCC
 365 reflections ($\{111\}_\gamma$, $\{200\}_\gamma$, $\{220\}_\gamma$, $\{311\}_\gamma$) and BCC reflections ($\{110\}_\delta$, $\{200\}_\delta$, $\{211\}_\delta$) were
 366 calculated to measure volume percent of austenite during heat treatment. It was determined
 367 that in the as-built condition, the amount of δ embed in the austenite matrix ranged between

36884 and 89 % (refer to the starting point in Figure 10 a). These differences in the ferrite content
 369 can be explained by the recursive alternation between vermicular and lathy ferrite in the
 370 samples before heat treatment, which may vary the content of ferrite. So, if the beam is
 371 analyzing a slightly different region on the material, minor changes in the δ -ferrite amount can
 372 occur.

373 The volume percent of undissolved δ -ferrite was higher in the PWHT performed at 1050 °C
 374 than in the PWHT at 1200 °C (Figure 10 b). The undissolved amount of ferrite was
 375 approximately 6.5 % and 0.4 %, respectively. The continuous increase in the volume percent of
 376 austenite during isothermal holding at 1050 °C suggests that two hours were not enough to
 377 reach an equilibrium state, since thermodynamic equilibrium calculations (refer to Table 5)
 378 predict a complete dissolution of the ferrite phase at 1050 °C, and a residual amount of 2.6 %
 379 at 1200 °C. Two potential concurrent effects can explain this: i) the heat treatment time was
 380 not enough to reach an equilibrium condition; ii) the segregation of alloying elements during
 381 WAAM can locally change the material's chemistry, delaying the dissolution kinetics [50]. After
 382 solubilization at 1200 °C, only the stable $\{211\}_\delta$ peak is observed, indicating a texture
 383 modification.



385 Figure 10 - a) Austenite volume percent during 1050 °C 2h and 1200 °C 1h; b) $\{200\}_\delta$ reflection
 386 before and after solubilization heat treatment.

387 The final fraction of δ -ferrite after the heat treatment decreases with an increase in the
 388 solubilization temperature. The complete dissolution of δ -ferrite in austenitic stainless steels
 389 can be hard to achieve since long heat treatment schedules are required [19,51].

390 Table 4 presents a comparison of the volume fraction measurements made using equations
 391 1,2,3 vs the Rietveld refinement method. A maximum deviation of 0.62 % was measured,
 392 proving that the method used to measure the volume fraction when only two phases are

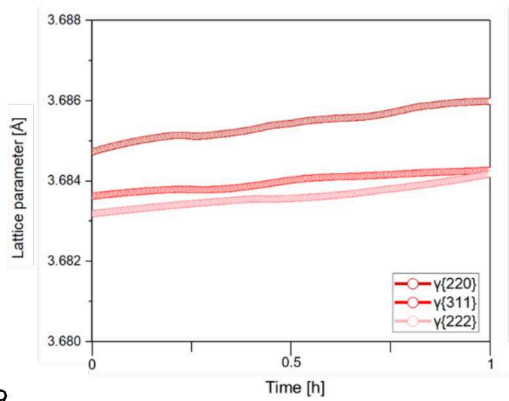
393 presented is valid. Moreover with MAUD it was possible to calculate 15.7 % as the final volume
 394 fraction of σ in the sample heat-treated at 950 °C. The fact that the final volume fraction of σ
 395 (15.74 %) is practically the same as the initial δ -ferrite volume fraction measured for the as-
 396 built condition (15.75 %), allows us to conclude that δ -ferrite acted as a nucleation site for the
 397 precipitation of σ . The precipitation of σ was restricted to the δ -ferrite segregation zones, and
 398 no δ -ferrite dissolution to the austenite matrix occurred. These results are also in good
 399 agreement with the ones already presented in Table 2, which measured phase percentage
 400 based on the micrographs characteristics.

401 *Table 4 - Comparison of the volume percent [%] of each phase after each heat treatment.*
 402 *Measurements were made via the single peak fitting method (equations: (1), (2) and (3)) vs*
 403 *Rietveld refinement method with MAUD.*

Phase	Austenite		δ - Ferrite		σ	
	Single peak fitting	MAUD	Single peak fitting	MAUD	Single peak fitting	MAUD
As-built	83.75	84.25	16.25	15.75	n.a.	n.a.
After 400 °C 1h	83.90	83.6	16.1	16.40	n.a.	n.a.
After 950 °C 2h	Not measured	84.26	n.a.	n.a.	Not measured	15.74
After 1050 °C 2h	93.5	94.12	6.5	5.88	n.a.	n.a.
After 1200 °C 1h	99.7	99.54	0.3	0.46	n.a.	n.a.

404

405 The lattice parameters calculated from the lattice spacing (d-spacing) for different {hkl} planes
 406 are given for the higher intensity peaks of austenite in Figure 11. During isothermal holding at
 407 1200 °C, the lattice parameter expands, which is attributed to the dissolution of ferrite that
 408 changes the austenite composition [52,53].



409

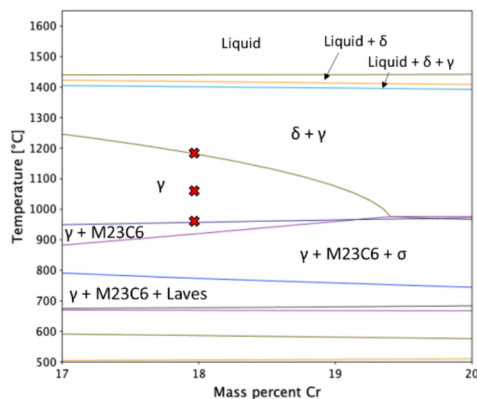
410 Figure 11 – Lattice parameter evolution of the most prominent FCC peaks during heat-
 411 treatment at 1200 °C.

412 Thermodynamic equilibrium calculations based on the TCFE11 database of Thermo-Calc (Table
 4135) were used to predict the equilibrium phases of the steel using the nominal composition in
 414 Table 1. Figure 12 depicts the equilibrium phase diagram with isopleths for each equilibrium
 415 phase as a function of temperature and the Cr mass percentage. Red crosses mark the ER
 416 316LSi composition for each heat treatment temperature. It should be noticed that some
 417 discrepancies between the X-ray diffraction results and the equilibrium CalPhaD-based
 418 calculations exist. At 400 °C it is expected a 5% volume fraction of Laves, which was not found
 419 either by high-energy X-ray diffraction or microscopic analysis. Since the effect of each heat
 420 treatment largely depends on the initial microstructure, the thermodynamic calculations do
 421 not take into account the as-built microstructure of large δ -ferrite dendrites but rather the
 422 material's nominal composition, which at 400 °C hindered the formation of laves. Laves
 423 precipitation is very sluggish and may occur over extended heat treatment times at 400 °C.
 424 Padilha et al. [44] showed that Laves only precipitates at 550 °C after 10 000 hours.
 425 Additionally, σ is not expected to exist above 900 °C, thus the observed σ at 950 °C during and
 426 after the heat treatment is in a metastable equilibrium state. Since δ -ferrite is
 427 thermodynamically metastable at temperatures where the σ precipitates, σ will preferentially
 428 grow from within the δ -ferrite causing its decomposition [49]. When the temperature rises to
 429 1050 and 1200 °C the system evolves into an equilibrium state by solubilizing the δ -ferrite. The
 430 experimentally observed residual δ -ferrite at 1050 and 1200 °C is not related to an equilibrium
 431 phase (formed above 1200 °C), but instead to insufficient decomposition. This can be explained
 432 since the selected heat treatment conditions are not equilibrium conditions: i. e. the chosen
 433 time for the post-WAAM heat treatment is not enough to reach an equilibrium condition.

434 Table 5 – Equilibrium calculations using TCFE11 database of Thermo-Calc for the volume
 435 percent [%] at the equilibrium temperatures of interest.

T [°C]	Austenite	δ - Ferrite	σ	Laves	M ₂₃ C ₆
400 °C	72	23	-	5	-
950 °C	99.95	-	-	-	0.05
1050 °C	100	-	-	-	-
1200 °C	97.4	2.6	-	-	-

436



437

438 Figure 12 - Calculated isopleth for Cr mass percentage. The red crosses mark the composition of
 439 ER 316LSi at each heat treatment temperature. The thermodynamic information is taken from
 440 the commercial thermodynamic database TCFE11.

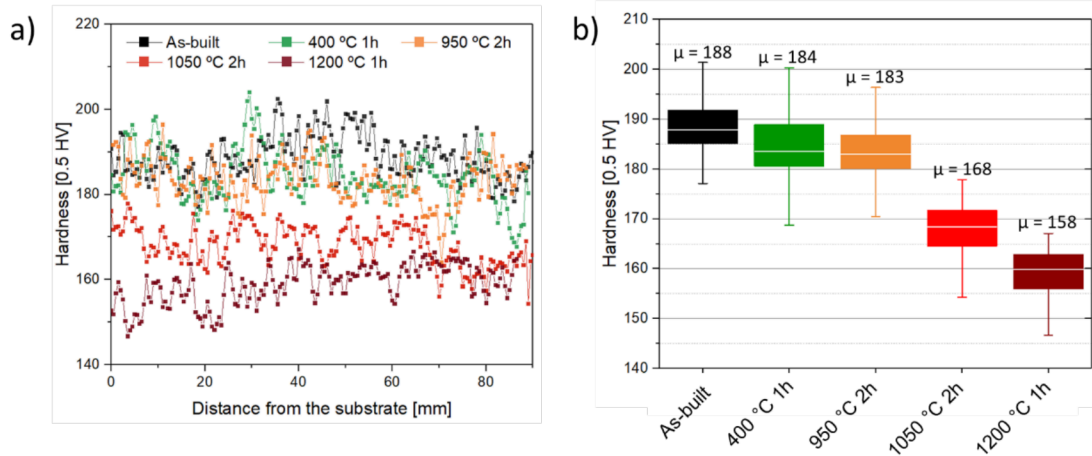
441 3.4 Hardness measurements

442 Vickers hardness plots as a function of distance from the substrate are presented in Figure 13.

443 As it can be seen, the higher hardness corresponds to the as-built and stress relieved sample
 444 (400 °C 1h), ranging from 170 to 200 HV. Higher temperatures resulted in a more significant
 445 dissolution of δ-ferrite, and therefore in lower hardness values. A maximum of 174 HV is
 446 observed for the heat-treated sample at 1050 °C, while a maximum of 163 HV was found in
 447 samples heat-treated at 1200 °C. Even though there is none δ-ferrite on the sample heat-
 448 treated at 950 °C, the slight difference between the means of this sample with the as-built
 449 condition is explained by the similar hardness of the σ in comparison to that of δ-ferrite.

450 The stress-relieved sample had similar hardness values with the non-stress-relieved one and
 451 can be explained by the multiple thermal cycles developed during sample build-up. After one
 452 layer is built, it is subjected to considerable periods at temperatures between 300-500 °C, thus
 453 experiencing an in-situ (at least partial) stress-relieving mechanism during production. The

454 more predominant variable to affect the hardness is, therefore, the amount of δ ferrite, as the
 455 hardness values obtained for the two different solubilization temperatures are lower than for
 456 the other heat treatment conditions



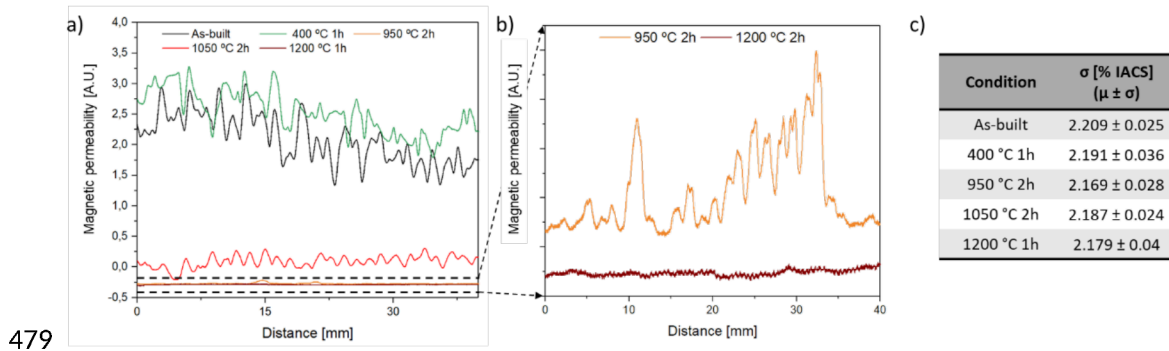
457

458 Figure 13 – a) Hardness measurements across sample's height, b) Boxplot of the hardness
 459 measurements displaying the minimum, maximum, median, and quartiles (Q1 and Q3) of each
 460 condition.

461 3.5 Electrical conductivity and magnetic permeability 462 measurements

463 Eddy current testing (ECT) and four-point probe technique were used to evaluate magnetic
 464 permeability and electrical conductivity changes, respectively. Results are depicted in Figure
 465 14. An inverse relation between the amount of δ -ferrite and the magnetic permeability was
 466 verified with ECT. With the gradual decrease of δ after PWHT at 1050 and 1200 °C, the signal
 467 output decreased. δ -ferrite is responsible to increase the magnetic permeability of the
 468 material, but sigma is not since it is not ferromagnetic. If there were not any X-ray diffraction
 469 measurements, δ -ferrite and σ could be qualitatively identified using ECT, as the microstructure
 470 images (Figure 4 b and d) do not allow to identify which constituents are present. The results
 471 show that the magnetic permeability of the samples containing δ (as-built and heat-treated at
 472 400 °C for 1h) is three times higher than the sample that includes the σ (heat-treated at 950 °C
 473 2h). The technique is very sensitive to variations of magnetic permeability, thus, variations in
 474 the δ -ferrite amount, however, very small variations of the electrical impedance were
 475 measured, as shown in Figure 14 b).

476 The average measurements of the electrical conductivity of these samples are between 2.169
 477 and 2.209 %IACS. The high standard deviation does not allow to establish any relationship
 478 between the amount of ferrite in a sample and the phases in it or with the grain size.



480 Figure 14 - a) Output signal of Eddy Current Testing (ECT) probe at 1.1 MHz, b) Detailed view of
 481 the signal output of ECT delineated with dashed lines, c) Average electrical conductivity
 482 measurements with a four-point probe for each condition.

483 Conclusions

484 A comprehensive study on the effect of post-WAAM heat treatments applied on 316L stainless
 485 steel was performed. By combining advanced microstructure characterization and in-situ
 486 measurements the following are the major findings of this work:

- 487 • The as-built WAAM samples presented an austenitic matrix with skeletal-type δ -ferrite
 488 and lathy-ferrite aligned with the solidification direction (z-axis). No other secondary
 489 phases were discernible.
- 490 • After the stress relief at 400°C, the microstructure retained similar characteristics to
 491 that of the as-built condition. Synchrotron X-ray diffraction showed that both the δ -
 492 ferrite and austenite peaks shifted to lower scattering angles, evidencing a change in
 493 microstrain. This heat treatment decreased the sample hardness by an average of 4 HV.
- 494 • There is no clear morphological difference between the as-built sample and sample
 495 heat-treated at 950 °C for two hours. However, by electron backscatter diffraction, it
 496 was confirmed that δ -ferrite acted as a nucleation site for the precipitation of
 497 undesirable σ -phase. The precipitation of the σ -phase was geometrically restricted to
 498 the δ -ferrite segregation zones.
- 499 • In-situ observations showed that σ precipitation started within the first minutes of
 500 isothermal holding at 950 °C, and two hours was enough to fully transform $\delta \rightarrow \sigma$. A
 501 hardness decreased of 5 HV relative to the as-built sample was achieved.

- 502 • Thermodynamic calculations do not predict the existence of σ in the sample heat-
503 treated at 950 °C. Insufficient kinetics for δ -ferrite dissolution led to a metastable
504 equilibrium condition, where σ replaced the former vermicular δ -ferrite structures
- 505 • A temperature of 1050 °C showed to be enough to promote ferrite dissolution and
506 compositional redistribution into the austenitic matrix, avoiding the precipitation of
507 metastable σ . Efficient dissolution of δ -ferrite dendrites can be achieved with higher
508 solubilization temperature, as heat treatments performed at 1050 and 1200 °C resulted
509 in approximately 6.5 % and 0.4 % of δ -ferrite, respectively.
- 510 • Eddy's current testing was shown to be able to distinguish σ from δ -ferrite in the
511 stainless steel WAAM parts. These results are promising for in-situ inspections of large
512 as-built components that cannot be easily segmented or transported.

513

514 **Acknowledgments**

515 TAR acknowledges FCT - MCTES for funding the Ph.D. grant SFRH/BD/144202/2019. VD
516 acknowledges FCT - MCTES for funding the Ph.D. grant SFRH/BD/139454/2018. TAR, JS, VD,
517 TGS, and JPO acknowledge Fundação para a Ciência e a Tecnologia (FCT - MCTES) for its
518 financial support via the project UID/00667/2020 (UNIDEMI). The São Paulo Research
519 Foundation partially financed this study (FAPESP), grant No. 2019/00691-0. The authors
520 acknowledge DESY (Hamburg, Germany), a member of the Helmholtz Association HGF, for the
521 provision of experimental facilities. Beamtime was allocated for proposals I-20181084 EC and I-
522 20191506. The research leading to this result has been supported by the project CALIPSOplus
523 under the Grant Agreement 730872 from the EU Framework Programme for Research and
524 Innovation HORIZON 2020.

525 **References**

- 526 [1] S.J. Zinkle, G.S. Was, Materials challenges in nuclear energy, *Acta Mater.* 61 (2013) 735–
527 758. <https://doi.org/10.1016/j.actamat.2012.11.004>.
- 528 [2] S.K. Lee, S.H. Yun, H.G. Joo, S.J. Noh, Deuterium transport and isotope effects in type
529 316L stainless steel at high temperatures for nuclear fusion and nuclear hydrogen
530 technology applications, *Curr. Appl. Phys.* 14 (2014) 1385–1388.
531 <https://doi.org/10.1016/j.cap.2014.08.006>.

- 532[3] M. Ziętała, T. Durejko, M. Polański, I. Kunce, T. Płociński, W. Zieliński, M. Łazińska, W.
533 Stępniewski, T. Czujko, K.J. Kurzydłowski, Z. Bojar, The microstructure, mechanical
534 properties and corrosion resistance of 316 L stainless steel fabricated using laser
535 engineered net shaping, *Mater. Sci. Eng. A.* 677 (2016) 1–10.
536 <https://doi.org/10.1016/j.msea.2016.09.028>.
- 537[4] Y. Dai, X. Zheng, P. Ding, Review on sodium corrosion evolution of nuclear-grade 316
538 stainless steel for sodium-cooled fast reactor applications, *Nucl. Eng. Technol.* 53 (2021)
539 3474–3490. <https://doi.org/10.1016/j.net.2021.05.021>.
- 540[5] Q. He, F. Pan, D. Wang, H. Liu, F. Guo, Z. Wang, Y. Ma, Microstructure and properties of
541 316L stainless steel foils for pressure sensor of pressurized water reactor, *Nucl. Eng.*
542 *Technol.* 53 (2021) 172–177. <https://doi.org/10.1016/j.net.2020.06.006>.
- 543[6] R.K. Desu, H. Nitin Krishnamurthy, A. Balu, A.K. Gupta, S.K. Singh, Mechanical properties
544 of Austenitic Stainless Steel 304L and 316L at elevated temperatures, *J. Mater. Res.*
545 *Technol.* 5 (2016) 13–20. <https://doi.org/https://doi.org/10.1016/j.jmrt.2015.04.001>.
- 546[7] H.P. Seifert, S. Ritter, H.J. Leber, Corrosion fatigue crack growth behaviour of austenitic
547 stainless steels under light water reactor conditions, *Corros. Sci.* 55 (2012) 61–75.
548 <https://doi.org/10.1016/j.corsci.2011.10.005>.
- 549[8] F.L. Xu, J.Z. Duan, C.G. Lin, B.R. Hou, Influence of Marine Aerobic Biofilms on Corrosion
550 of 316L Stainless Steel, *J. Iron Steel Res. Int.* 22 (2015) 715–720.
551 [https://doi.org/10.1016/S1006-706X\(15\)30062-5](https://doi.org/10.1016/S1006-706X(15)30062-5).
- 552[9] M.M. DEWIDAR, K.A. KHALIL, J.K. LIM, Processing and mechanical properties of porous
553 316L stainless steel for biomedical applications, *Trans. Nonferrous Met. Soc. China*
554 (English Ed. 17 (2007) 468–473. [https://doi.org/10.1016/S1003-6326\(07\)60117-4](https://doi.org/10.1016/S1003-6326(07)60117-4).
- 555[10] X. Lou, M.A. Othon, R.B. Rebak, Corrosion fatigue crack growth of laser additively-
556 manufactured 316L stainless steel in high temperature water, *Corros. Sci.* 127 (2017)
557 120–130. <https://doi.org/10.1016/j.corsci.2017.08.023>.
- 558[11] J.P. Oliveira, T.G. Santos, R.M. Miranda, Revisiting fundamental welding concepts to
559 improve additive manufacturing: From theory to practice, *Prog. Mater. Sci.* 107 (2020)
560 100590. <https://doi.org/10.1016/j.pmatsci.2019.100590>.

- 561[12] V.R. Duarte, T.A. Rodrigues, N. Schell, R.M. Miranda, J.P. Oliveira, T.G. Santos, Hot
562 Forging Wire and Arc Additive Manufacturing (HF-WAAM), *Addit. Manuf.* (2020)
563 101193. <https://doi.org/10.1016/j.addma.2020.101193>.
- 564[13] J.A. Brooks, F.J. Lambert, Effects of Phosphorus, Sulfur and Ferrite Content on Weld
565 Cracking of Type 309 Stainless Steel., *Weld. J. (Miami, Fla)*. 57 (1978).
- 566[14] A. Ben Rhouma, T. Amadou, H. Sidhom, C. Braham, Correlation between microstructure
567 and intergranular corrosion behavior of low delta-ferrite content AISI 316L aged in the
568 range 550–700 °C, *J. Alloys Compd.* 708 (2017) 871–886.
569 <https://doi.org/10.1016/j.jallcom.2017.02.273>.
- 570[15] J.C. Lippold, W.F. Savage, Solidification of Austenitic Stainless Steel Weldments - 3. the
571 Effect of Solidification Behavior on Hot Cracking Susceptibility., *Weld. J. (Miami, Fla)*. 61
572 (1982) 388–396.
- 573[16] P.D. Jablonski, J.A. Hawk, Homogenizing Advanced Alloys: Thermodynamic and Kinetic
574 Simulations Followed by Experimental Results, *J. Mater. Eng. Perform.* 26 (2017) 4–13.
575 <https://doi.org/10.1007/s11665-016-2451-3>.
- 576[17] T.A. Rodrigues, V. Duarte, J.A. Avila, T.G. Santos, R.M. Miranda, J.P. Oliveira, Wire and arc
577 additive manufacturing of HSLA steel: Effect of thermal cycles on microstructure and
578 mechanical properties, *Addit. Manuf.* 27 (2019).
579 <https://doi.org/10.1016/j.addma.2019.03.029>.
- 580[18] T.F. de Andrade, A.M. Kliauga, R.L. Plaut, A.F. Padilha, Precipitation of Laves phase in a
581 28%Cr-4%Ni-2%Mo-Nb superferritic stainless steel, *Mater. Charact.* 59 (2008) 503–507.
582 <https://doi.org/10.1016/j.matchar.2007.03.006>.
- 583[19] A. Perron, C. Toffolon-Maslet, X. Ledoux, F. Buy, T. Guilbert, S. Urvoy, S. Bosonnet, B.
584 Marini, F. Cortial, G. Texier, C. Harder, V. Vignal, P. Petit, J. Farré, E. Suzon, Understanding
585 sigma-phase precipitation in a stabilized austenitic stainless steel (316Nb) through
586 complementary CALPHAD-based and experimental investigations, *Acta Mater.* 79 (2014)
587 16–29. <https://doi.org/10.1016/j.actamat.2014.06.066>.
- 588[20] M.J. Cieslak, A.M. Ritter, W.F. Savage, Chi-Phase Formation During Solidification and
589 Cooling of Cf-8M Weld Metal., *Weld. J. (Miami, Fla)*. 63 (1984).

- 590[21] A.D. Warren, I.J. Griffiths, P.E.J. Flewitt, Precipitation within localised chromium-
591 enriched regions in a Type 316H austenitic stainless steel, *J. Mater. Sci.* 53 (2018) 6183-
592 6197. <https://doi.org/10.1007/s10853-017-1748-4>.
- 593[22] D.M. Escriba, E. Materna-Morris, R.L. Plaut, A.F. Padilha, Chi-phase precipitation in a
594 duplex stainless steel, *Mater. Charact.* 60 (2009) 1214-1219.
595 <https://doi.org/10.1016/j.matchar.2009.04.013>.
- 596[23] X. Chen, J. Li, X. Cheng, B. He, H. Wang, Z. Huang, Microstructure and mechanical
597 properties of the austenitic stainless steel 316L fabricated by gas metal arc additive
598 manufacturing, *Mater. Sci. Eng. A.* 703 (2017) 567-577.
599 <https://doi.org/10.1016/j.msea.2017.05.024>.
- 600[24] P. Long, D. Wen, J. Min, Z. Zheng, J. Li, Y. Liu, Microstructure evolution and mechanical
601 properties of a wire-arc additive manufactured austenitic stainless steel: Effect of
602 processing parameter, *Materials (Basel)*. 14 (2021).
603 <https://doi.org/10.3390/ma14071681>.
- 604[25] D.M.E. Villanueva, F.C.P. Junior, R.L. Plaut, A.F. Padilha, Comparative study on sigma
605 phase precipitation of three types of stainless steels: Austenitic, superferritic and
606 duplex, *Mater. Sci. Technol.* 22 (2006) 1098-1104.
607 <https://doi.org/10.1179/174328406X109230>.
- 608[26] C.-C. Hsieh, W. Wu, Overview of Intermetallic Sigma (σ) Phase Precipitation in Stainless
609 Steels, *ISRN Metall.* 2012 (2012) 1-16. <https://doi.org/10.5402/2012/732471>.
- 610[27] K.W. Chan, S.C. Tjong, Effect of secondary phase precipitation on the corrosion behavior
611 of duplex stainless steels, *Materials (Basel)*. 7 (2014) 5268-5304.
612 <https://doi.org/10.3390/ma7075268>.
- 613[28] V.S. Raghunathan, V. Seetharaman, S. Venkadesan, P. Rodriguez, The influence of post
614 weld heat treatments on the structure, composition and the amount of ferrite in type
615 316 stainless steel welds, *Metall. Trans. A.* 10 (1979) 1683-1689.
616 <https://doi.org/10.1007/BF02811701>.
- 617[29] C. Arganis, N.F. Garza-montes-de-oca, Original article Sensitization of an austenitic
618 stainless steel due to the occurrence of δ -ferrite, (2018).
619 <https://doi.org/10.1515/corrrev-2018-0036>.

- 620[30] Q. Chao, S. Thomas, N. Birbilis, P. Cizek, P.D. Hodgson, D. Fabijanic, The effect of post-
621 processing heat treatment on the microstructure, residual stress and mechanical
622 properties of selective laser melted 316L stainless steel, *Mater. Sci. Eng. A.* 821 (2021)
623 141611. <https://doi.org/10.1016/j.msea.2021.141611>.
- 624[31] N. Chen, G. Ma, W. Zhu, A. Godfrey, Z. Shen, G. Wu, X. Huang, Enhancement of an
625 additive-manufactured austenitic stainless steel by post-manufacture heat-treatment,
626 *Mater. Sci. Eng. A.* 759 (2019) 65–69. <https://doi.org/10.1016/j.msea.2019.04.111>.
- 627[32] D. Kong, C. Dong, X. Ni, L. Zhang, J. Yao, C. Man, X. Cheng, K. Xiao, X. Li, Mechanical
628 properties and corrosion behavior of selective laser melted 316L stainless steel after
629 different heat treatment processes, *J. Mater. Sci. Technol.* 35 (2019) 1499–1507.
630 <https://doi.org/10.1016/j.jmst.2019.03.003>.
- 631[33] A.N.F.& D.H. A. P. Hammersley, S. O. Svensson, M. Hanfland, Two-dimensional detector
632 software: From real detector to idealised image or two-theta scan, *High Press. Res.*
633 14:4–6 (1996) 235–248. <https://doi.org/10.1080/08957959608201408>.
- 634[34] P. Crowther, C. Daniel, xrdfit: A Python package for fitting synchrotron X-ray diffraction
635 spectra, *J. Open Source Softw.* 5 (2020) 2381. <https://doi.org/10.21105/joss.02381>.
- 636[35] J.D. Escobar, G.A. Faria, L. Wu, J.P. Oliveira, P.R. Mei, A.J. Ramirez, Austenite reversion
637 kinetics and stability during tempering of a Ti-stabilized supermartensitic stainless steel:
638 Correlative in situ synchrotron x-ray diffraction and dilatometry, *Acta Mater.* 138 (2017)
639 92–99. <https://doi.org/10.1016/j.actamat.2017.07.036>.
- 640[36] L. Lutterotti, R. Vasin, H.R. Wenk, Rietveld texture analysis from synchrotron diffraction
641 images. I. Calibration and basic analysis, *Powder Diffr.* 29 (2014) 76–84.
642 <https://doi.org/10.1017/S0885715613001346>.
- 643[37] T.G. Santos, R.M. Miranda, P. Vilaça, J.P. Teixeira, J. dos Santos, Microstructural mapping
644 of friction stir welded AA 7075-T6 and AlMgSc alloys using electrical conductivity, *Sci.*
645 *Technol. Weld. Join.* 16 (2011) 630–635.
646 <https://doi.org/10.1179/1362171811Y.0000000052>.
- 647[38] G.L. Sorger, J.P. Oliveira, P.L. Inácio, N. Enzinger, P. Vilaça, R.M. Miranda, T.G. Santos,
648 Non-destructive microstructural analysis by electrical conductivity: Comparison with
649 hardness measurements in different materials, *J. Mater. Sci. Technol.* 35 (2019) 360–

- 650 368. <https://doi.org/10.1016/j.jmst.2018.09.047>.
- 651[39] E.G. Astafurova, M.Y. Panchenko, V.A. Moskvina, G.G. Maier, S. V. Astafurov, E. V.
652 Melnikov, A.S. Fortuna, K.A. Reunova, V.E. Rubtsov, E.A. Kolubaev, Microstructure and
653 grain growth inhomogeneity in austenitic steel produced by wire-feed electron beam
654 melting: the effect of post-building solid-solution treatment, *J. Mater. Sci.* 55 (2020)
655 9211–9224. <https://doi.org/10.1007/s10853-020-04424-w>.
- 656[40] J.W. Elmer, S.M. Allen, T.W. Eagar, Microstructural development during solidification of
657 stainless steel alloys, *Metall. Trans. A.* 20 (1989) 2117–2131.
658 <https://doi.org/10.1007/BF02650298>.
- 659[41] N. Suutala, T. Takalo, Austenitic Stainless Steel Welds, *Metall. Trans. A. I* (1980) 717–725.
- 660[42] J.W. Fu, Y.S. Yang, J.J. Guo, Formation of a blocky ferrite in Fe-Cr-Ni alloy during
661 directional solidification, *J. Cryst. Growth.* 311 (2009) 3661–3666.
662 <https://doi.org/10.1016/j.jcrysgr.2009.05.007>.
- 663[43] A. F. PADILHA, P. R. RIOS, Decomposition of Austenite in Austenitic Stainless Steels, *ISIJ*
664 *Int.* 42 (2002) 325–337.
- 665[44] A.F. Padilha, D.M. Escriba, E. Materna-Morris, M. Rieth, M. Klimenkov, Precipitation in
666 AISI 316L(N) during creep tests at 550 and 600 °C up to 10 years, *J. Nucl. Mater.* 362
667 (2007) 132–138. <https://doi.org/10.1016/j.jnucmat.2006.12.027>.
- 668[45] J.R.Y. T.H. Chen, Effects of solution treatment and continuous cooling on γ -phase
669 precipitation in a 2205 duplex stainless steel, *J. Nucl. Mater.* 311 (2006) 220.
- 670[46] J.W. Elmer, T.A. Palmer, E.D. Specht, Direct observations of sigma phase formation in
671 duplex stainless steels using In-situ synchrotron X-ray diffraction, *Metall. Mater. Trans. A*
672 *Phys. Metall. Mater. Sci.* 38 (2007) 464–475. [https://doi.org/10.1007/s11661-006-9076-](https://doi.org/10.1007/s11661-006-9076-3)
673 [3](https://doi.org/10.1007/s11661-006-9076-3).
- 674[47] J.P. Oliveira, F.M.B. Fernandes, R.M. Miranda, N. Schell, J.L. Ocaña, Residual stress
675 analysis in laser welded NiTi sheets using synchrotron X-ray diffraction, *Mater. Des.* 100
676 (2016) 180–187. <https://doi.org/10.1016/j.matdes.2016.03.137>.
- 677[48] B. Rivolta, R. Gerosa, F. Tavasci, The dilatometric technique for studying sigma phase
678 precipitation kinetics in F55 steel grade, *J. Therm. Anal. Calorim.* 132 (2018) 869–877.

679 <https://doi.org/10.1007/s10973-017-6940-x>.

680[49] S. Atamert, J.E. King, Sigma-phase formation and its prevention in duplex stainless
681 steels, *J. Mater. Sci. Lett.* 12 (1993) 1144–1147. <https://doi.org/10.1007/BF00420548>.

682[50] A. Caballero, J. Ding, S. Ganguly, S. Williams, Wire + Arc Additive Manufacture of 17-4
683 PH stainless steel: Effect of different processing conditions on microstructure, hardness,
684 and tensile strength, *J. Mater. Process. Technol.* 268 (2019) 54–62.
685 <https://doi.org/10.1016/j.jmatprotec.2019.01.007>.

686[51] T.P.S. Gill, M. Vijayalakshmi, J.B. Gnanamoorthy, K.A. Padmanabhan, Transformation of
687 Delta-Ferrite During the Postweld Heat Treatment of Type 316L Stainless Steel Weld
688 Metal., *Weld. J. (Miami, Fla.)*. 65 (1986) 122–128.

689[52] A. Bénéteau, P. Weisbecker, G. Geandier, E. Aeby-Gautier, B. Appolaire, Austenitization
690 and precipitate dissolution in high nitrogen steels: An in situ high temperature X-ray
691 synchrotron diffraction analysis using the Rietveld method, *Mater. Sci. Eng. A*. 393
692 (2005) 63–70. <https://doi.org/10.1016/j.msea.2004.09.054>.

693[53] D. Manova, S. Mändl, H. Neumann, B. Rauschenbach, Analysis of in situ XRD
694 measurements for low energy ion beam nitriding of austenitic stainless steel, *Surf.*
695 *Coatings Technol.* 256 (2014) 64–72. <https://doi.org/10.1016/j.surfcoat.2014.03.047>.

696